journal of the American Ceramic Society

Crystallization Kinetics of LaF3 Nanocrystals in an Oxyfluoride Glass

Journal:	*Journal of the American Ceramic Society*
Manuscript ID:	JACERS-29195.R1
Manuscript Type:	Article
Date Submitted by the Author:	n/a
Complete List of Authors:	De Pablos, Araceli; CSIC, Instituto de Cerámica y Vidrio Hemono, Nicolas; CSIC, Instituto de Cerámica y Vidrio Mather, Glenn; CSIC, Instituto de Cerámica y Vidrio Bhattacharyya, Sommnath; Tata Institute of Fundamental Research, Department of Condensed Matter Physics and Materials Science Hoche, Thomas; Leibniz-Institut für Oberflächgenmodifizierung e.V Bornhöft, Hansjörg; Institut für Nichtmetallische Werkstoffe Deubener, Joachim; Institut für Nichtmetallische Werkstoffe Munoz, Francisco; CSIC, Instituto de Cerámica y Vidrio Duran, Alicia; CSIC, Instituto de Cerámica y Vidrio Pascual, Maria; CSIC, Instituto de Cerámica y Vidrio
Keywords:	glass-ceramics, nanomaterials, crystals/crystallization

Crystallization Kinetics of LaF_3 Nanocrystals in an Oxyfluoride Glass

A. de Pablos-Martín[1], N. Hémono[1], G.C. Mather[1], S.Bhattacharyya[2,3], T. Höche[2], H.Bornhöft[4], J.Deubener[4], F. Muñoz[1], A. Durán[1], M.J. Pascual[1]

[1]*Instituto de Cerámica y Vidrio (CSIC), Kelsen 5, 28049 Madrid, Spain*

[2]*Leibniz-Institut für Oberflächgenmodifizierung e.V., Permoserstraße 15, D-04318 Leipzig, Germany*

[3] *Department of Condensed Matter Physics and Materials Science, Tata Institute of Fundamental Research, Mumbai 400005, India*

[4]*Institut für Nichtmetallische Werkstoffe, TU-Clausthal, Clausthal-Zellerfeld, Germany*

Abstract

Nanocrystallization of LaF_3 in a glass of composition $55SiO_2$-$20Al_2O_3$-$15Na_2O$-$10LaF_3$ (mol %) has been achieved by heat treatment above the glass transition temperature. A maximum crystal size of 14 nm has been attained, with the crystalline fraction and crystal size dependent on the time and temperature of thermal treatment. The effect of lanthanum fluoride crystallisation is noticeable from the microstructural and compositional changes in the glass matrix, which have been studied using several techniques, including viscosity, dilatometry, X-ray diffraction (XRD) and quantitative Rietveld refinement, transmission electron microscopy (TEM) and differential scanning calorimetry (DSC). The crystallisation mechanism is shown to occur via regions of La- and Si-phase separation in the glass, from which the fluoride crystals develop during heat treatment. The interface between the glass matrix and the crystals in the demixed ranges is enriched in network formers, mainly SiO_2, creating a viscous barrier, which inhibits further crystal growth and limits the crystal size to the nanometric range.

Keywords: Oxyfluoride glasses; Glass-ceramics; Crystallisation; Nano-crystals; LaF_3

1. Introduction

Glass-ceramics containing nanoscaled crystals are key materials for photonic applications due to their low phonon energy and optical transparency. Oxyfluoride glass matrices are of particular interest since they combine the high chemical durability associated with oxide glasses with the high solubility of rare-earth cations and transparency offered by fluoride crystals [1-6]. Lanthanum fluoride glass-ceramics are excellent candidates for photonic applications [7-12] due to their ability to host rare-earth ions in crystalline precipitates in which the phonon energy is very low. If the optically active ion is incorporated into the fluoride crystalline phase, the intensity of the characteristic laser emission is enhanced. Ideally, the crystal size should be in the range 5–100 nm, with a narrow size distribution in order to minimize scattering losses. The crystallisation of a fluoride phase is achieved by heat treatment slightly above the glass transition temperature (T_g). The base glass composition, the temperature and the time of heat treatment will influence the crystallisation process, and the resulting phase composition, crystal size, volume concentration and distribution.

Since a pre-requisite for optical applications is the high transparency of glass-ceramics, the crystallites must be nanosized and present a narrow crystal-size distribution. Knowledge of their preparation and a better understanding of the crystallization mechanism are, therefore, of considerable importance. Theories of crystallization are usually restricted to isochemical systems in which the crystalline phase has the same chemical composition as the glass matrix. However, the challenge of obtaining large volume concentrations of crystals, with sizes in the nanometric range and a narrow size distribution, can only be achieved in multicomponent systems in which the interface formed during nucleation and crystal growth is controlled. In highly viscous liquids, such as glass melts near the glass transition

temperature, this leads to a locally altered chemical composition at the interface between the crystalline precipitates and their surrounding matrix. For coupled processes of viscosity and crystal growth, two cases can be distinguished: (i) the viscosity of the liquid at the interface is smaller than that of the bulk, leading to an increase in the crystal growth rate due to enhanced diffusion; (ii) the viscosity increases, such that the interface acts as a diffusional barrier which decelerates the crystal-growth velocity. With regard to this latter scenario, Rüssel [13] suggested a mechanism for the crystallisation of CaF_2, in which crystallisation takes place starting from a homogeneous glass. The formed interface is enriched in glass formers increasing viscosity near the crystals, with the effect that a diffusional barrier forms around each crystal, which hinders further crystal growth. This mechanism was later confirmed by Bocker *et al*. [14], who described the crystallization of BaF_2 in a similar glass matrix, and Bhattacharrya et al. [15] who discussed the impact of such diffusion barriers on the action of nucleation agents in lithia-aluminosilicate glass ceramics. Hémono *et al*. [16,17] studied LaF_3 nanocrystallisation and its characterisation by TEM in similar glasses, indicating that phase separation precedes crystallisation. The application of transmission electron microscopy for the investigation of glasses and glass-ceramics in general was recently reviewed by Höche [18]; the advantages of employing energy-filtered transmission electron microscopy (EFTEM) for the study of enrichment zones in glass ceramics is described in detail by Bhattacharyya *et al*. [16,19]. ^{19}F-NMR experiments of both phase-separated an non-phase-separated glasses showed that La-F or Ba-F bonds are already present in the parent glass and diffusion of fluoride takes place from the glass to the crystal when crystallisation progresses [20, 21].

Knowledge of the crystallization mechanism of lanthanum fluoride nano-glassceramics is fundamental in order to design improved materials. In this paper, the process of crystallization of an oxyfluoride glass in which LaF_3 precipitates has been analysed in

detail, employing dilatometry, viscometry, DSC, XRD, and TEM to study the mechanism of nanocrystallization.

2. Experimental

2.1. Glass melting, crystallisation and chemical analysis

A glass with composition $55SiO_2.20Al_2O_3.15Na_2O.10LaF_3$ (mol %) was prepared by melting reagent grade SiO_2 (Saint-Gobain, 99.6%), Al_2O_3 (Panreac, calcined for 12 h at 800°C), Na_2CO_3 (Panreac, 99.5%) and LaF_3 (Panreac, 99%). Batches were firstly calcined for 2 h at 1200 °C and then melted during 1.5 h at 1600 °C. The batches were quenched twice in air onto a brass mould in order to obtain homogeneous transparent glasses. Glass-ceramics were obtained by controlled crystallisation of LaF_3 on heat treatments at temperatures between T_g + 35 °C and T_g + 95 ºC for various time lengths.

Samples were analysed by X-ray Fluorescence Spectroscopy (XRF) with a Panalytical spectrometer. The content of all oxides was determined employing the melting method with $Li_2B_4O_7$; the fluorine content was analysed employing pressed pellets of powdered glass (8 g) in order to avoid volatilization.

2.2 X-ray diffraction

Phase analysis of glass-ceramics obtained after thermal treatment at 620 ºC for different lengths of time were conducted using powder XRD with a D-5000 Siemens diffractometer using monochromatic Cu Kα radiation (λ = 1.5406 Å). Patterns were scanned over the angular range $20 \leq 2\theta \leq 60°$ with a step size of 0.05° and a fixed counting time of 2.5 s/step.

Glass-ceramics obtained at 660 ºC and 680 ºC, from 1 to 80 h, were studied by XRD using an X'Pert PRO Panalytical diffractometer equipped with an X´Celerator detector. The patterns were collected with monochromatic Cu Kα radiation over the range $10 \leq 2\theta \leq 70°$ with a step size of 0.0167° and a fixed counting time 200 s/step.

The crystallized fraction of LaF_3 on prolonged thermal treatment (620 ºC, 40 h) was estimated by quantitative Rietveld analysis of XRD data, employing a similar method to that applied to a similar glass-ceramic with nanocrystals [22] and other largely amorphous multiphase materials [23]. The glass was ground to a fine powder in an agate mortar, sieved through a 60 μm mesh then milled again with NaF (PRO-VYS, 99.9%), which was used as internal standard in a suitable quantity (3 wt.%) to approximate the peak intensity of the crystalline LaF_3. The average particle size of the NaF internal standard was determined to be 11.4 μm using the laser light dispersion method with a Mastersizer S instrument (Malver Instruments Ltd.). XRD powder data for Rietveld analysis were collected over the range $10° \leq 2\theta \leq 110°$ with a stepwidth of 0.02° and a fixed counting time of 4 s/step, employing a Bruker TT diffractometer equipped with a Lynx Eye detector and monochromatic Cu Kα radiation. Rietveld refinement was carried out with the FULLPROF program [24] using interpolation of background points to model the amorphous contribution to the pattern.

2.3 Transmission electron microscopy

Samples of the oxy-fluoride glasses and glass-ceramics for TEM were prepared by cutting slices, plane-parallel grinding, dimpling to a residual thickness of 10 to 15 μm, and ion-beam thinning using Ar^+ ions. Overheating of the TEM foils and the consequent introduction of artefacts was avoided by means of double-sided, ion-beam etching at small angles (< 6 °) and low etching energies (acceleration voltage, 2.5 kV; beam current < 8

μA).The non-conducting sample was selectively coated with carbon prior to TEM investigation [25] in order to reduce electrostatic charging under the electron beam.

TEM samples were characterised in two transmission electron microscopes. Conventional TEM imaging and diffraction was performed at an acceleration voltage of 75 keV in a Hitachi H-8100 instrument (point-to-point resolution: 0.23 nm), EFTEM imaging was performed in a Zeiss EM 912 microscope (c_s=2.7 mm, c_c=2.7 mm, Köhler illumination), operating at 120 kV (LaB_6 filament) and equipped with an in-column Omega-type energy filter. Elemental maps were generated using the three-window technique [26] only for regions that obeyed Crozier's conditions [27], i.e., multiple scattering effects are negligible. The energy-window width was 10 eV for the La-$N_{4,5}$ /Si-$L_{2,3}$ map. Digital micrograph software (Gatan Inc., Pleasanton, CA, USA) was used for image processing.

2.4 Dilatometry and differential scanning calorimetry

Glass transition temperatures (T_g) and coefficients of thermal expansion (CTE) were determined by dilatometry at a heating rate of 10 K/min in air using a Netzsch Gerätebau dilatometer, model 402 EP.

DSC measurements were performed with a Setaram instrument (Model Setsys Evolution 16/18) using powdered Al_2O_3 as inert reference material and employing 100–150 mg of glass with particle size of 1– 1.25 mm in order to reproduce bulk conditions. The DSC scans were carried out with heating rates in the range 5 – 40 K/min in order to determine the activation energy for crystallisation and the Avrami parameter, *n*. In addition, peak crystallisation temperatures of glass samples previously heat treated during 1 h within the temperature range, T_g +10 – T_g+135 ºC, were monitored by heating samples through the

crystallization temperature range at 10 K/min in order to identify a possible optimum nucleation temperature.

2.5 Viscosity

The viscosity of the glass was determined using the procedures of fibre elongation and rotation in melted glass, employing a high-temperature Haake viscometer equipped with a ME 1700 sensor. The fibre-elongation method was performed in the interval 10^{12} – 10^{7} Pa.s according to International Standard IS0 7884-3, using loads of 2 – 250 g, depending on the viscosity. Fibres were prepared with diameter 0.6 – 0.8 mm and a length of 50 ± 2 mm with a ball at each extreme, in accordance with rule DIN 52 312 part 3. The viscosity at each temperature and time was determined for at least three samples using different weights. The maximum error in the viscosity determination was log η ± 0.1. In order to study the influence of crystallization on viscosity, some fibres were thermally treated at 620, 640 and 660 ºC for different time lengths (20 - 80 h) and the viscosity was measured at 660 ºC.

The rotation procedure was applied for viscosity in the range 10^{3} – 10^{1} Pa.s using a high-temperature rotation viscometer of the cylindrical Searle type at rotation speeds of 1–30 rpm for 10 min, following the International Standard ISO 7884-2. Three measurements were taken at three different rotation speeds for each temperature within this range. The use of both methods allows determination of the complete viscosity-temperature curve.

Hot-Stage Microscopy (HSM) was performed in a Leica-EM201 microscope with image analysis for determination of the viscosities in air at a heating rate of 5 K/min. The samples were initially cold pressed to conformed bodies of 3 mm in both height and diameter from glass powder with a particle size < 60 μm. The temperature was measured with a Pt/Rh (6130) thermocouple placed under and in contact with the alumina support. The temperatures

corresponding to the characteristic viscosity points, following Scholze's definition [28, 29], were obtained from photomicrographs.

Indentation methods allow the viscosity to be determined at a certain temperature as a function of time. Micro-indentation measurements were performed on a vertical dilatometer (Bähr VIS 404, Hüllhorst, Germany) by force control at 10 N and using a pushing rod which was equipped with a sapphire micro-sphere of radius 0.75 mm. Samples with coplanar surfaces and height of ca. 5 mm were prepared by grinding and polishing. Viscometer runs were carried out at ambient atmosphere at 620, 660 and 680 ºC for 5 h, employing a heating rate of 10 K/min. After a dwell time for thermal equilibration and structural relaxation, the weight was loaded on the pushing rod and the sphere started to penetrate the glass surface. For measurements at 620 and 660 ºC, the applied weight was 500 g and for 680 ºC it was 300 g. A linear variable displacement transducer continuously recorded the indentation depth of the sphere into the glass. The micropenetration viscometer was calibrated using a standard glass (G1) of PTB (Physikalisch-Technische Bundesanstalt, Germany). The certified viscosity data [30] could be reproduced with an accuracy of 0.02 (rotation) and 0.1 (micropenetration) in log units [31].

3. Results and discussion

The nominal and analysed compositions of the oxyfluoride glass are summarized in Table 1. The fluorine loss during melting in air is around 38 %, similar to that observed in another composition of the same system [22]. The glass transition temperature of the oxyfluoride glass was 585 ± 2ºC.

Figure 1 shows the variation of the glass transition temperature as a function of the heat treatment time at 620 ºC. T_g increases by 60 K within the first 20 h, and then remains

almost constant for longer treatment times. The initial increase is explained by the depletion of fluoride ions in the glass matrix due to the crystallization of LaF_3, developing an enrichment of network former ions in the residual glassy matrix, which leads to an increase in T_g. For time lengths > 20 h, the crystallization process is finalized and the structure of the glass matrix does not change significantly, resulting in a slight decrease in T_g. All the glass-ceramics heated according to the detailed regimes were transparent.

3.1 X-ray diffraction and the crystallization process

The XRD patterns of the glass-ceramics after treatments at 620 ºC for time lengths ranging from 1 to 80 h are shown in Fig. 2. The reflections of the crystallized fraction were consistent with those of hexagonal lanthanum fluoride LaF_3 (PDF file No. 32-0483). The crystallization of LaF_3 was detected after 1 h of treatment at 620 °C, with the peak intensity increasing with further treatment time. The size of the crystals was calculated from the (111) peak of LaF_3 ($2\theta \approx 27.5°$) using the Scherrer equation:

$$D = \frac{G\lambda}{B\cos\theta} \quad (1)$$

where D is the crystal size, G is a constant whose value is 0.9, B is the corrected full width at half maximum of the peak and θ is the Bragg angle. The errors were calculated by peak fitting and in accordance with error theory. The crystal size increased in the measured temperature range from 5 to 10 nm, as shown in Fig. 3.

In order to analyse more thoroughly the crystallization mechanism as a function of time and temperature of treatment, two further crystallization kinetics at 660 and 680 ºC were carried out from 1 to 80 h. All glass-ceramics were transparent, except those obtained at 680

ºC for times longer than 40 h. Crystal sizes, as calculated by the Scherrer equation, increased non-linearly (Fig. 3). The time-dependence of the crystal size in Fig.3 was, therefore, fitted according to

$$r = Ut^p \quad (2)$$

giving,

$$\log(r) = \log(U) + \mathrm{p}\,\log(t) \quad (3)$$

where r is the average crystal radius, U is the growth rate, t is the dwell time, and p is the growth exponent. Figure 4 shows the time dependence of r in double logarithmic scales. The growth exponent p was found to be very small (≤ 0.17). Practically no crystal growth was detected for dwell times > 10 h, where the value of p was close to zero. As discussed in more detail later, the arrest of the crystal growth is related to the formation of a viscous SiO_2 layer around the crystals during heat treatment, which acts as diffusion barrier inhibiting crystal growth. At higher temperatures such as 680°C, it is observed that the diffusional barrier is overcome and coarsening of the crystals in the demixed areas occurs. At these temperatures, the viscosity decreases and the crystal growth rate increases, thus the diffusional barrier is less efficient for preventing crystal growth and the crystals are able to grow more. On the other hand, the formation of agglomerates is also expected at higher temperatures with increasing annealing time, which leads to the loss of transparency in the glass-ceramics [17].

Quantitative Rietveld Analysis

Structural models of LaF_3 (space group, $P\bar{3}c1$) and the NaF internal standard ($Fm\bar{3}m$) were refined by Rietveld analysis based on published structural data [32, 33]. LaF_3 is known to crystallize in hexagonal platelets [34]. The effects of the crystal shape on the diffraction data were incorporated in the Rietveld refinement by allowing the independent refinement of the profile parameters of certain "special reflections" in Fullprof, e.g. (002), which are subject to broadening. The thermal vibration factors of the two phases were not refined in order to avoid correlation with the background or other parameters [35]. The observed diffraction pattern and the difference pattern between observed and calculated data on termination of Rietveld refinement are shown in Fig. 5. Final structural parameters and reliability factors indicating the quality of the refinement are listed in Table 2.

The weight fraction of LaF_3 obtained by refinement was corrected for the presence of the amorphous phase from the X-ray and real weight fractions of the NaF internal standard with the same procedure as outlined in previous works [22, 23]. The actual weight fraction of LaF_3 in the glass, after correction for the presence of the NaF standard in the refinement data, was calculated to be ~ 7.3 wt%. Absorption contrast effects (microabsorption) of phase mixtures with different linear absorption coefficients may influence the X-ray diffraction intensities and the results of the quantitative analysis. Brindley [36] classified the absorption effects in mixed powders on the basis of the value of μD where μ is the linear absorption coefficient and D is the particle size. In the present case, the LaF_3 nanocrystals and NaF internal standard may be classified as fine powders ($\mu D < 0.01$) on the basis of their weighted absorption coefficients and particle sizes such that no microabsorption correction need be applied.

3.2. TEM

A TEM micrograph of the base glass collected at 75 keV is shown in Fig. 6a, which reveals liquid-liquid phase-separation droplets enriched in elements of high atomic number (strong scattering). The droplets are fully amorphous and with an average diameter in the range 30 – 40 nm, as determined by electron diffraction (not shown).

The average size of the phase-separation droplets did not change significantly after annealing for 40 h at 620 °C (Fig. 6b). However, the shape of the droplets became less spherical as a result of the formation of LaF_3 crystallites (cf. XRD results presented in Section 3.1). The crystallites are of smaller diameter than the droplets such that up to four crystallites can coexist within a droplet. As is the case for glasses with different fractions of lanthanum and silicon [16], TEM and EDX analyses indicate that the phase-separation droplets contain not only lanthanum and fluorine but also silicon and oxygen, in addition to traces of aluminium. It may be assumed, therefore, that on annealing the growth of the LaF_3 crystallites within the droplets is limited to some extent by an excess of silicon. On termination of the crystallization process, several LaF_3 nanocrystals of ca. 9 nm in diameter are formed, which are trapped in a volume determined by the size of the preceding liquid-liquid phase-separation droplets. The remaining volume of this former droplet is filled with the excess of Si, Al and O, as has been observed previously in a $40SiO_2.30\ Al_2O_3.18\ Na_2O.12\ LaF_3$ (mol %) glass [16]. In order to verify this hypothesis, energy filtered TEM was employed. A silicon elemental map was obtained with the three-windows technique [26] using images from two pre-edge windows centred at 77 eV and 87 eV, and one post-edge window centred at 109 eV. The calculated spatial resolution of this image is ≈ 3 nm using cc =2.7 mm [37]. Since the Si-$L_{2,3}$ and La-$N_{4,5}$ edges are very close to each other, the latter cannot be excluded as having an effect on the intensity distribution in the Si map; the existence of La is supported by an

EFTEM simulation presented previously for the $Na_2O–Al_2O_3– SiO_2–LaF_3$ system [22]. In order to confirm the presence of La in the nanocrystals, it would have been instructive to acquire a La elemental map using the La-$M_{4,5}$ edge at 832 eV as, in this case, there is no superimposed contribution from Si ; however, this was not possible due to the high sensitivity of the specimen to the electron beam and the unfavorable signal-to-noise ratio.

There is a difference in the manner in which the silica-enriched region is formed around the crystals in phase-separated and non-phase-separated glasses. In a non-phase-separated parent glass, such as the CaF_2- or BaF_2-containing glasses studied by Rüssel [13, 14], fluorides precipitate from a homogeneous glass. The silica enrichment around the formed crystals induces an increase of viscosity which limits further crystal growth. For a phase-separated parent glass like the title composition, droplets are present, which, in the present case, are rich in lanthanum and silicon. Further thermal treatment of the glass results in the growth of LaF_3 crystals inside the droplets, while silicon redistributes itself around the crystals forming a shell, which then inhibits further crystal growth. Nevertheless, as mentioned in the introduction, in both types of glass, La-F bonds (presumably in the phase-separated droplets) or Ba-F bonds are already present in the parent glasses, and F diffusion from the glass matrix to the crystal has been demonstrated in both cases.[20, 21].

3.3. DSC

The DSC results at different heating rates are shown in Fig. 7. The glass transition temperature is identified as the point of intersection of the two tangents of the depression in the baseline of the curves. The crystallization peak corresponds to LaF_3 crystallization. Table 3 lists the T_g and the temperature of the crystallisation peak, T_p, at different heating rates.

Determination of the Avrami exponent was performed using Avrami's law

$$x = 1\text{-}\exp[\text{-}(kt)^n] \quad (4)$$

where x is the volume fraction crystallised after time t, and n is the Avrami exponent. The apparent reaction rate, k, is usually assigned an Arrhenius temperature dependence

$$k = k_0 \exp(\text{-}E/RT) \quad (5)$$

where E is the activation energy describing the overall crystallisation process.

Rearranging eq. (5):

$$\ln[\text{-}\ln(1\text{-}x)] = n \ln k + n \ln t \quad (6)$$

The crystallized volume x may be calculated from the ratio of the partial area at a certain temperature to the total area of the exothermic crystallization peak. The values of n are, thus, directly determined by plotting $\ln[\text{-}\ln(1\text{-}x)]$ versus $\ln t$. It should be noted that eq. (4) strictly applies to isothermal conditions. However, the relation is commonly modified to describe non-isothermal crystallization for which experimental studies are easier to conduct. Yinnon and Uhlmann [38] have summarized several different treatments for non-isothermal conditions based on eqs. (4) and (6) assuming a constant heating rate Q. On this basis, plotting $\ln[\text{-}\ln(1\text{-}x)]$ versus $\ln Q$ at a fixed temperature yields n from the Ozawa equation (7):

$$\left.\frac{\mathrm{d}[\ln[\text{-}\ln(1\text{-}x)]]}{\mathrm{d}[\ln Q]}\right|_T = -n \quad (7)$$

Values of n were calculated according to eq. (7) from the plot shown in Fig. 8 for a quantity of x associated with the temperature range 660 – 680 ºC. Table 4 summarizes the Avrami parameters determined from figure 8a, with an average value of $n \approx 1$.

To determine the apparent activation energy for crystallization, the data obtained using different heating rates in figure 7 can be analyzed assuming two alternative scenarios: (1) that crystal growth occurs at a fixed number of nuclei; (2) that further nuclei are formed during the DSC measurement.

In the first situation, either the Kissinger , Takhor or Augis-Bennett (KTAB) equations can be applied, respectively given as

$$\ln(Q/T_P^{\,2}) = -E/RT_P + A \tag{8}$$

$$\frac{d[\ln Q]}{d[1/T_p]} = \frac{E}{R} \tag{9}$$

and

$$\frac{d[ln(Q/(T_p - T_0))]}{d[1/T_p]} = \frac{E}{R} \tag{10}$$

where T_p is the temperature of the maximum of the crystallization peak in K, Q is the heating rate, T_0 is the temperature at the beginning of the experiment in K, R is the gas constant, E is the activation energy of the overall crystallization process, including nucleation and crystal-growth phenomena and A is a constant. Figure 9a shows the plots obtained using these equations, of which the Kissinger relation (eq. (8)) is the most representative.

For the second scenario, where further nuclei are formed during the DSC measurement, the Matusita equation (11) may be applied:

$$\ln(Q^n / T_P^2) = -mE / RT_P + A \quad (11)$$

where m represents the dimensionality of crystal growth and determines which equation is correct in each case: If $m = n$, crystallization occurs at a fixed number of nuclei and the Kissinger equation can be applied, whereas if $m = n-1$, nucleation occurs during the DSC experiment and the Matusita relation is more appropriate.

In the present work, E/n was first obtained from the Marseglia equation (12):

$$\ln(Q / T_P) = -(E / nRT_P) \quad (12)$$

The value of n obtained from the Ozawa equation allows the activation energy E to be calculated from a plot of the Marseglia relation (Figure 9b), from which m can also be determined.

The activation energies obtained from the various relations are summarized in Table 4. The E value determined from the KTAB-equation (eq. (10)) approaches 338 kJ/mol, equivalent to that determined from the Marseglia equation (eq. (12)). The value of m, 0.85, approaches a value of 1, and is very similar to that obtained for n (0.99). According to Donald [39] such values of m and n can correspond to a bulk crystallization mechanism with a constant number of nuclei (i.e. a well nucleated sample in which the number of nuclei is independent of the heating rate). Crystal growth occurs in two dimensions with a crystal size growth rate $\sim\sqrt{t}$ (diffusion controlled), as expected for LaF_3 nanoplates [34]. For this type of mechanism, where $m \approx n \approx 1$, adoption of the Kissinger equation (eq.(10)) is correct.

DSC scans collected at 10 K/min of the glasses treated at different nucleation temperatures for one hour are shown in Fig. 10. If effective nucleation takes place during thermal treatment, a decrease in the crystallization peak should be observed with respect to the untreated glass. However, the crystallization peaks appear at higher temperatures and are of lower area on increasing the nucleation temperature. This is due to the fact that, during thermal treatment for 1 hour, crystallization originates from the previously formed nuclei and no additional nuclei are formed. Even for the glass treated at higher nucleation temperatures, 670 – 720 ºC, no crystallization peak is observed because all the glass has already been crystallized during the thermal treatment. This observation is consistent with the crystallization mechanism proposed from the values of the *m* and *n* parameters, which involves crystallization originating from a constant number of nuclei located at the La- and F-rich phase-separation droplets in the base glass, as shown in the TEM analysis of the samples [11].

3.4. Viscosity

The viscosity-temperature curve using the isokom temperature T_{12} (for which the Newtonian viscosity is 10^{12} Pa.s) as scaling parameter of the glass is shown in Fig. 11. The viscosity was determined from points obtained by different methods: T_g (measured by DSC) corresponds to a viscosity of log η = 12.0 Pa.s, the three highest viscosity points were obtained by the fibre-elongation method (log η=12-7 Pa.s), and four intermediate points were determined on the basis of photographs from hot-stage microscopy (HSM). The last method [29] defines some fixed viscosity points as follows: first shrinkage (log η= 7.9), maximum shrinkage (log η= 6.9), half ball (log η= 3.5) and flow (log η= 2.1). The rotation method was also used for log η < 3 Pa s. The temperature dependence of viscosity was fitted using the

empirical Vogel-Fulcher-Tammann (VFT) [40-42] and Avramov-Milchev (AM) [43] equations, employing exclusively the rotation-viscometry and T_g data in order to ensure the absence of immiscibility and crystallization effects, which are expected to be insignificant at temperatures up to glass transition and above the liquidus.

According to the VFT equation

$$\log \eta = A_1 + \frac{B_1}{T - C_1} \tag{13}$$

the parameters were fitted as A_1 = -5.7 ± 0.07, B_1 = 11713 ± 1720 and C_1 = 197 ± 13 (Pa.s, K). On employing the AM relation

$$\log \eta = A_2 + B_2 \left(\frac{T_g}{T} \right)^{C_2} \tag{14}$$

the fitting parameters were determined as A_2 = -4.3 ± 0.86, B_2 = 16.35 ± 0.93 and C_2 = 1.4 ± 0.1 (Pa.s, K).

A physically based viscosity model involving the temperature dependence of configurational entropy has recently been introduced by Mauro-Yue-Ellison-Gupta-Allen (MYEGA) [44]:

$$\log \eta = A_3 + \frac{B_3}{T} \exp\left(\frac{C_3}{T} \right) \tag{15}$$

Fitting of this relation gives A_3 = -5.6 ± 0.8, B_3 = 11186 ± 1749 and C_3 = 256 ± 96 (Pa.s, K). Figure 11 shows that Eqs. 13-15 fitted the data equally. Transformation kinetics in the

temperature range from T_g to the liquidus seem not to influence viscosity for the short period of heat treatment used for hot-stage microscopy.

In order to classify the energetic character of liquids, Angell [45] introduced kinetic fragility expressed by the steepness index m at the glass transition

$$m = \left. \frac{d(\log \eta)}{d\left(\frac{T_g}{T}\right)} \right|_{T=Tg} \tag{16}$$

This relation provides a measure of the deviation from Arrhenian temperature dependence. From Angell's plot (Fig. 11), it is apparent that the viscosity of the examined oxyfluoride glass (m = 22) lies between two extremes referred to as ''strong" (e.g. tetrahedral networks such as SiO_2 and GeO_2, $m \approx 17$) and ''fragile" (e.g. nitrate melt, $m \approx 100$).

The fibre-elongation method was used in order to analyze the effects of liquid-liquid phase separation and subsequent crystallization of lanthanum fluoride on viscosity. Fibres were thermally pre-treated for prolonged time lengths, i.e. at 620 ºC for 20 and 80 h, 640 ºC for 20 h and 660º C for 20 h, subsequent to viscosity measurement at 660 ºC. Effective viscosity increased by up to one order of magnitude with both dwell temperature and dwell time of the pre-treatment (Fig. 12). Time-dependent viscosity measurements were also performed by micro-indentation. The increase in viscosity with dwells at 620, 660 and 680 ºC for 1.5 to 7 h is shown in Fig. 13. Assuming a linear increase in the logarithm of the effective viscosity with crystal volume fraction for dilute systems [46] and a constant number of crystals, the slope of a straight line through the data is given by $3p$. Values of p were determined as 0.22 (620 °C), 0.18 (660 °C) and 0.16 (680 °C), which are close to those determined from the increase in crystal size (eq. (1) and Fig. 4). A relative viscosity value up

to 15 (Fig. 12) for a crystallized volume fraction of around 7.3 % (neglecting small changes in density of the two liquids) indicates that the increase in effective viscosity is attributable to a factor other than suspended crystals. A relative viscosity up to 2 has been determined for spherical and plate-like, micro-sized crystals in silicate melts, where the crystal phase and the glass matrix had the same chemical composition or crystals act as quasi inert filler [47]. The large value of the relative viscosity shown in Fig. 12 is, thus, assumed to reflect liquid-liquid phase separation, which probably changes the chemical composition of the matrix melt towards one of higher flow resistance. Demixing of a network modifier-rich glass composition (lanthanum fluoride) will initially lead to soft amorphous inclusions, which will gradually become more rigid as crystallization proceeds in the demixed droplets. However, we assume that the effects of changes in melt composition on effective viscosity are much greater than those of dispersed soft/rigid inclusions. The strong increase in glass transition, as determined by dilatometry (Fig. 1), provides supporting evidence for this hypothesis since glass transition mainly reflects the change in thermal expansion of the continuous matrix phase, as also observed in CaF_2 and BaF_2 compositions [13, 14].

4. Conclusions

Transparent LaF_3-oxyfluoride glass-ceramics with LaF_3 nano-crystals up to 14 nm in diameter were obtained from thermal treatments of $55SiO_2.20Al_2O_3.15Na_2O.10LaF_3$ (mol %) glass at temperatures from T_g + 35 to T_g + 95 ºC. Changes in the microstructure due to phase separation and subsequent fluoride crystallization, with a crystalline mass fraction up to 7.3 wt.%, were made evident by several techniques.

The glass transition temperature increased with treatment time at 620 ºC, indicating enrichment in network formers in the glassy matrix and subsequent fluorine crystallisation. The limited variation of crystal size on treatment from 1 to 80 h at 620, 660 and 680 ºC

indicated a low crystal growth velocity which decreased close to zero with the time of treatment. TEM and EDXS analyses indicate that the phase-separation droplets contain not only lanthanum and fluorine but also silicon and oxygen, in addition to traces of aluminium. It may be assumed, therefore, that, on annealing, the growth of the LaF_3 crystallites within the droplets is limited to some extent by an excess of silicon. On termination of the crystallization process, several LaF_3 nanocrystals are formed, which are trapped in a volume determined by the size of the preceding liquid-liquid phase-separation droplets. The remaining volume of this former droplet is filled with the excess of Si, Al and O. Diffusional barriers and the confinement to the demixed ranges in which fluoride crystallizes are assumed to freeze the crystal growth at crystal sizes smaller than demixed droplets. The change in composition in the glass matrix due to demixing, subsequent crystal growth and the minimal effect of suspended volume fraction were confirmed by an increase in viscosity of up to an order of magnitude with temperature and time of treatment at 620 ºC. The reason for the increase in viscosity has been demonstrated to be the same as that reported previously for CaF_2 and BaF_2 compositions in which crystallisation from a homogeneous glass takes place. The presence of nuclei in the base glass was confirmed by calculation of the Avrami parameter *n* from DSC data, which indicated bulk crystallization from a well-nucleated sample via a two-dimensional growth mechanism (nanoplates). Moreover, DSC curves performed at different nucleation temperatures revealed that crystallization takes place from preexisting active sites. The broadened profiles of certain reflections in the XRD data of the glass-ceramic provided supporting evidence for the growth of nanoplate-shaped crystals.

Acknowledgements

The authors acknowledge the financial support of Project INTERCONY, Contract No. NMP4-CT-2006-033200, from Framework 6 of the European Union, the CSIC incorporation intramural project 2007 60I002, and the CiCyt project MAT 2010-20459. A. De Pablos-Martín is grateful to CSIC for a JAE contract. The authors thank Eva Peiteado for her assistance with viscosity measurements.

Figure captions

Figure 1: Variation of the glass transition temperature as a function of dwell time at 620°C. The dashed line is a visual guide only.

Figure 2: XRD patterns of glass samples treated at 620 °C during (a) 0h, (b)1 h, (c) 3 h, (d) 30 h, (e) 40 h and (f) 80 h.

Figure 3: Variation of the crystal size of the glass-ceramics as a function of the time of heat treatment at 620, 660 and 680 °C as calculated on the basis of the (1 1 1) diffraction peak at 27.5° (2θ).

Figure 4: Time-dependent progress of the average crystal radius in double logarithmic scales. The lines provide best fits (Eq. 3) to the data. Numbers indicate growth index *p*.

Figure 5: Observed and difference X-ray powder diffraction profiles of glass-ceramic treated at 620 ºC for 40 h with 3 wt.% NaF as internal standard (reflections marked with asterisks).

Figure 6 : Zero-loss filtered bright-field TEM image of (a) the glass sample ,(b) the glass-ceramic obtained at 620 ºC for 40 h and (c) the corresponding La-$N_{4,5}$ /(Si-$L_{2,3}$) map.

Figure 7: DSC curves of the glass recorded from 5 to 40 K/min.

Figure 8: Ozawa plot constructed from DSC data from 660 to 680 ºC for the determination of the Avrami exponent n.

Figure 9: (a) ■ Kissinger, □ Takhor and ● Augis-Bennett plots constructed from the DSC data; (b) Marseglia and Matusita plots. Q is the heating rate and T_P is the DSC crystallisation peak.

Figure 10: DSC curves of the glass with nucleation temperatures from 595 to 720ºC recorded at a rate of 10 K/min.

Figure 11: Viscosity-temperature curve of the glass obtained from T_g point, hot-stage microscopy (HSM), fibre elongation and rotation methods. Curves were fitted according to the Vogel-Fulcher-Tamman (VFT), Avramov-Milchev (AM) and Mauro-Yue-Ellison-Gupta-Allen (MYEGA) equations.

Figure 12. Viscosity of the treated fibres as a function of temperature and time of treatment, measured at 660 ºC.

Figure 13: Viscosity as a function of isothermal dwelling at 620, 660 and 680 ºC measured by micro-indentation. Straight lines of slope 3*p* give the best linear fit to the data.

Table 1: Nominal and analyzed compositions (in mol %) of base glass

Glass Components	Nominal (mol %)	Analysed (mol %)
SiO_2	55	55.10
Al_2O_3	20	20.39
Na_2O	15	14.77
LaF_3	10	6.51
La_2O_3	0	3.23
F^- (wt %)	6.92	4.30

Table 2. Structure refinement data for LaF_3 nanocrystals

Space group $P\bar{3}c1$; a = 7.1926(3) Å, c = 7.3716(7) Å; R_p = 2.17; R_{wp} = 2.93; χ^2 = 2.74

Atom	*Site*	*x/a*	*y/b*	*c/z*	*occupancy*
La(1)	6f	0.6535(5)	0	1/4	1.0
F(1)	12g	0.332(8)	-0.001(5)	0.096(2)	1.0
F(2)	4d	1/3	2/3	0.133(2)	1.0
F(3)	2a	0	0	1/4	1.0

- * Thermal vibration factors were constrained to B_{iso} = 1.0

Table 3: T_g and T_p values at different heating rates obtained from the DSC curves in Fig.7

Q (*K/ min*)	T_g (ºC)±2 T_g (*Dilatometry*) = 585 °C	T_p (ºC) ±2
5	581	667
10	590	679
15	590	687
20	591	693
30	592	703
40	598	714

Table 4: The Avrami exponent of Ozawa's equation obtained from Fig. 7 and activation energies as determined from various relations.

Avrami parameter *n*			Activation Energy *Ea* (kJ/mol)			
T (°C)	**n**	**R²**	***Ln Q*** ***Takhor*** (R² = 0.992)	***Ln (Q/ T_p^2)*** ***Kissinger*** (R² = 0.9943)	***Ln (Q/(T_p-T_0))*** ***Augis-Bennett*** (R² = 0.990	***Ln (Q^n/T^2_p)*** ***Marseglia*** (R² = 0.990)
660	1.12	0.998	348 ± 23	330 ± 24	335 ± 24	338 ± 23
670	0.87	0.9996				
675	0.80	0.9993				
680	0.75	0.998				

References

1. F. Auzel, D. Pecile, D. Morin, "Rare Earth Doped Vitroceramics: New, Efficient, Blue and Green Emitting Materials for Infrared Up-Conversion", J. Electrochem. Soc. 122 101-107 (1975).
2. D. C Tran, G. H Sigel Jr., B. Bendow, "Heavy Metal Fluoride Glasses and Fibers: A Review", J. Lightwave Technolog. LT-2 5 566-586 (1984).
3. B. J. Ainslie, S. T. Davey, D. Szebesta, J. R. Williams, M.W. Moore, T.Whitley, R. Wyatt, "A review of fluoride fibres for optical amplification", J. Non-Cryst. Solids 184 225-228 (1995).
4. M. Yamada, T. Kanamori, Y. Terunuma, K. Oikawa, M. Shimizu, S. Sudo, K. Sagawa, "Fluoride-based erbium-doped fiber amplifier with inherently flat gain spectrum", IEEE Photon. Technol. Lett. 8 (7) 882-884 (1996).
5. E. Downing, L. Hesselink, J. Ralston, R. Macfarlane, "A Three-Color, Solid-State, Three-Dimensional Display", Science 273 (1996) 1185-1189.
6. Y. Wang, J. Ohwaki, "New transparent vitroceramics codoped with Er^{3+} and Yb^{3+} for efficient frequency upconversion", Appl. Phys. Lett. 63 [24] 3268-3270 (1993).
7. M.J. Dejneka, "The luminescence and structure of novel transparent oxyfluoride glass-ceramics", J. Non-Cryst. Solids 239 149-155 (1998).
8. R.E Youngman, M.J Dejneka, "NMR Studies of Fluorine in Aluminosilicate-Lanthanum Fluoride Glasses and Glass-Ceramics", J. Am. Ceram. Soc. 85 [5] 1077-1082 (2002).
9. S. Tanabe, H. Hayashi, T. Hanada, N. Onodera, "Fluorescence properties of Er^{3+} ions in glass ceramics containing LaF_3 nanocrystals", Opt. Mater. 19 343-349 (2002).
10. F. Goutaland, P. Jander, W.S Brocklesby, G. Dai, "Crystallisation effects on rare earth dopants in oxyfluoride glass ceramics", Opt. Mater. 22 383-390 (2003).

11. M. Reben, I. Waclawska, C. Paluszkiewicz, M. Środa, "Thermal and structural studies of nanocrystallisation of oxyfluoride glasses", J. Therm. Anal. Cal. 88 285-289 (2007).

12. M. Reben, I. Waclawska, "Structure and nanocrystallization of SiO_2-Al_2O_3-Na_2O-LaF_3 glasses", Proceedings of XXI International Congress on Glass, Strasbourg (France), July 2007.

13. Ch. Rüssel, "Nanocrystallization of CaF_2 from $Na_2O/K_2O/CaO/CaF_2/Al_2O_3/SiO_2$ glasses", Chem. Mater. 17 5843-5847 (2005).

14. Ch. Bocker, S. Bhattacharyya, Th. Höche, Ch. Rüssel, "Size distribution of BaF_2 nanocrystallites in transparent glass ceramics", Acta Mater. 57 5956–5963 (2009).

15. S. Bhattacharyya, Ch. Bocker, T. Heil, J.R. Jinschek, Th. Höche, Ch. Rüssel, H. Kohl, "Experimental Evidence of Self-Limited Growth of Nanocrystals in Glass", Nano Lett. 9 2493-2496 (2009).

16. S. Bhattacharyya, Th. Höche, N. Hemono, M.J. Pascual, P.A van Aken, "Nanocrystallization in LaF_3-Na_2O-Al_2O_3-SiO_2 glass", J. Cryst. Growth 311 [18] 4350-4355 (2009).

17. N. Hémono, G. Pierre, F. Muñoz, A. de Pablos-Martín, M.J. Pascual, A.Durán, "Processing of transparent glass-ceramics by nanocrystallisation of LaF_3", J. Eur. Ceram. Soc. 29 [14] 2915-2920 (2009).

18. Th. Höche, "Crystallization in Glass - Elucidating a Realm of Diversity by Transmission Electron Microscopy", J. Mater. Sci. 45 3683-3696 (2010).

19. S. Bhattacharyya, Th. Höche, K. Hahn, P.A. van Aken, "Various transmission electron microscopic techniques to characterize phase separation in inorganic glasses", J. Non-Cryst. Solids 355 393-396 (2009).

20. F. Muñoz, A.De Pablos-Martín, N.Hémono, M.J.Pascual, A.Durán, L.Delevoye, L.Montagne, "NMR investigation of the crystallization mechanism of LaF_3 and $NaLaF_4$ phases in aluminosilicate glasses", J. Non-Cryst. Solids 357 1463-1468 (2011).

21. C.Bocker, F.Muñoz, A.Durán, C.Rüssel, "Fluorine sites in glasses and transparent glass-ceramics of the system $Na_2O/K_2O/Al_2O_3/SiO_2/BaF_2$, J. Solid State Chem. 184 405-410 (2011).

22. A. de Pablos-Martín, G.C. Mather, F. Muñoz, S. Bhattacharyya, Th. Höche, J.R. Jinschek, T. Heil, A. Durán, M.J. Pascual, "Design of oxy-fluoride glass-ceramics containing $NaLaF_4$ nano-crystals", J. Non-Cryst. Solids 356 [52-54] 3071-3079, 2010.

23. X. Orlhac, C. Fillet, P. Deniard, A.M. Dulac, R. Brec, "Determination of the crystallized fractions of a largely amorphous multiphase material by the Rietveld method", J. Appl. Cryst. 34 114 (2001).

24. J. Rodriguez-Carvajal, Physica B 192 (1993) 55.

25. Th. Höche, J.W. Gerlach, T. Petsch, "Static-charging mitigation and contamination avoidance by selective carbon coating of TEM samples", Ultramicroscopy 106 981-985 (2006).

26. W. Jäger, J. Mayer, "Energy-Filtered Transmission Electron-Microscopy of Si_mGe_n Superlattices and Si-Ge Heterostrucures", Ultramicroscopy 59 [1-4] 33-45 (1995).

27. P.A. Crozier, "Quantitative Elemental Mapping of Materials by Energy-Filtered Imaging", Ultramicroscopy 58 (2) 157-174 (1995).

28. M.J. Pascual, L. Pascual, A. Durán, "Determination of viscosity-temperature curve for glasses, on the basis of fixed viscosity points determined by heating microscopy", Phys. Chem. Glasses, 42(1) 61-66 (2001).

29. M.J. Pascual, A. Durán, M.O. Prado, "A new method for determining fixed viscosity points of glasses", Phys. Chem. Glasses, 46 [5] 512-520 (2005).

30. N. Böse, G. Klingenberg, G. Meerlender, "Viscosity measurements of glass melts-Certification of reference material", Glastech. Ber., Glass Sci. Technol. 74 115-126 (2001).

31. J. Deubener, H. Bornhöft, S. Reinsch, R. Müller, J. Lumeau, L.N. Glebova, L.B. Glebov, "Viscosity, relaxation and elastic properties of photo-thermo-refractive glasses", J. Non-Cryst. Solids 355 126-131 (2009).

32. A. Zalkin, D. H. Templeton, "Refinement of the trigonal crystal structure of lanthanum trifluoride with neutron diffraction data"Acta Cryst. B 4191-93 (1985).

33. W.L. Bragg, Nature, "Crystal structure", 105 646-648 (1920).

34. Y. Tian, X. Jiao, J. Zhang, N. Sui, D.R. Chen, G.Y. Hong, "Molten salt synthesis of LaF_3:Eu^{3+} nanoplates with tunable size and their luminescence properties", J. Nanopart. Res. 12 [1] 161-168 (2010).

35. L.B. McCusker, R.B. von Dreele, D.E. Cox, D. Louër, P. Scardi, "Rietveld refinement guidelines, J. Appl. Cryst. 32 36-50 (1999).

36. G.W. Brindley, "The Effect of Grain or Particle Size on X-ray Reflections from Mixed Powders or Alloys", Phil. Mag. Series 7 [36] 347-369 (1945).

37. O.L. Krivanek, M.K. Kundmann, K. Kimoto, "Spatial resolution in EFTEM Elemental Maps", J. Micros. 180 277-287 (1995).

38. H. Yinnon, D.R. Uhlmann, "Applications of thermoanalytical techniques to the study of crystallization kinetics in glass-forming liquids", J. Non-Cryst. Solids 54 3 253-275 (1983).

39. I.W. Donald, "Crystallisation kinetics of a lithium zinc silicate glass studied by DTA and DSC", J. Non-Cryst. Solids, 120-6 345-346 (2004).

40. H. Vogel, "Temperature dependence of viscosity of melts", Physik. Z., 22, 645-6, 1921.

41. G.S. Fulcher, “Analysis of recent measurements of the viscosity of glasses”, J Am. Ceram. Soc., 8 339-55 1925.

42. G. Tammann, W. Hesse, “Temperature dependence of viscosity of melted supercooled liquids”, Anorg Chem., 156, 245-7 1926.

43. I. Avramov, A. Milchev, “Effect of disorder on diffusion and viscosity in condensed systems”, J. Non-Cryst. Solids, 104 253-260 (1988).

44. J.C. Mauro, Y. Yue, A.J. Ellison, P.K. Gupta, D.C. Allan, “Viscosity of glass-forming liquids”, Proceedings of the National Academy of Sciences U S A. 106 19780–19784 (2009).

45. C.A. Angell, “Relaxation in liquids, polymers and plastic crystals — strong/fragile patterns and problems”, J. Non-Cryst. Solids 131–133 13-31 (1991).

46. J. Deubener, R. Brückner, “Influence of nucleation and crystallization on the rheological properties of lithium disilicate melts”, J. Non-Cryst. Solids 209 96 – 111 (1997).

47. R. Müller, M. Eberstein, S. Reinsch, J. Deubener, A. Thiel, W. A. Schiller, “Effect of rigid inclusions on sintering of LTCC”, Phys. Chem. Glasses Eur. J. Glass Sci. Technol. B 48 259-266 (2007).

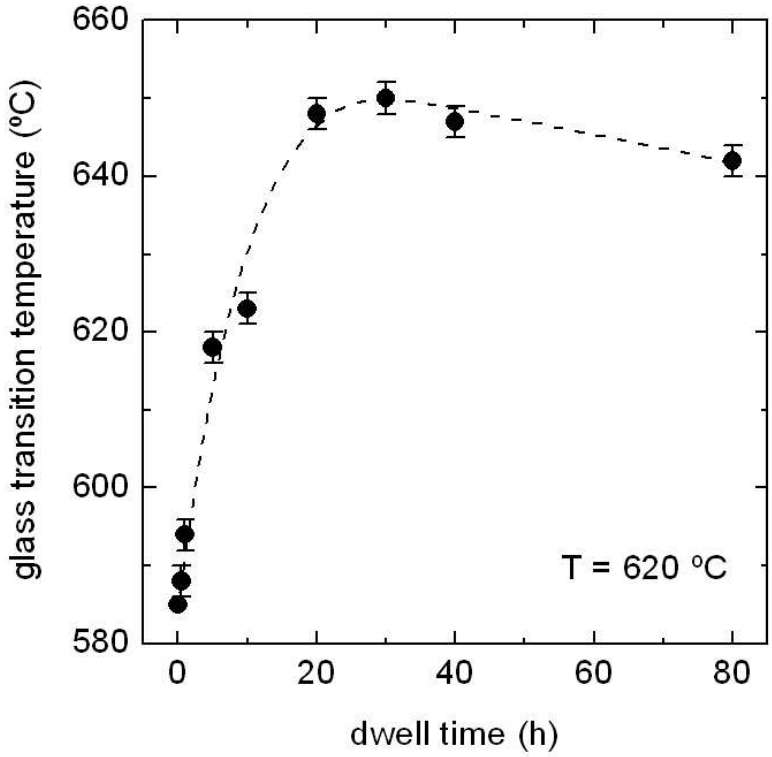

Figure 1: Variation of the glass transition temperature as a function of dwell time at 620°C. The dashed line is a visual guide only.
220x203mm (100 x 100 DPI)

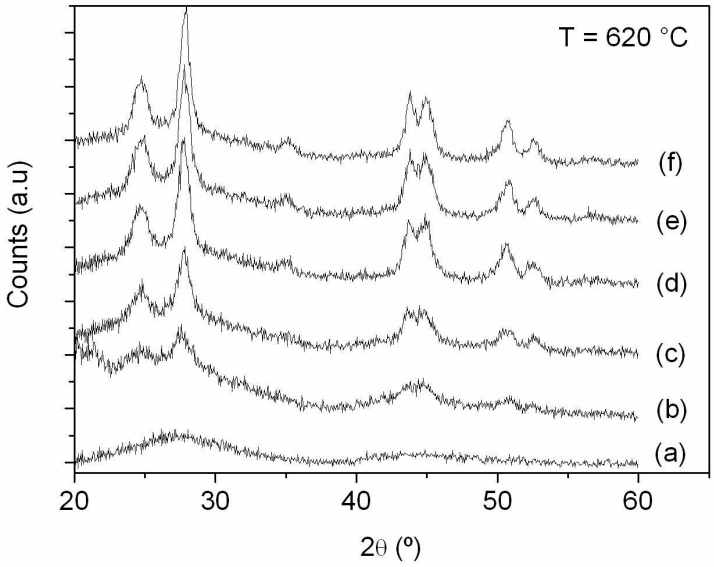

Figure 2: XRD patterns of glass samples treated at 620 °C during (a) 0h, (b)1 h, (c) 3 h, (d) 30 h, (e) 40 h and (f) 80 h.
290x203mm (150 x 150 DPI)

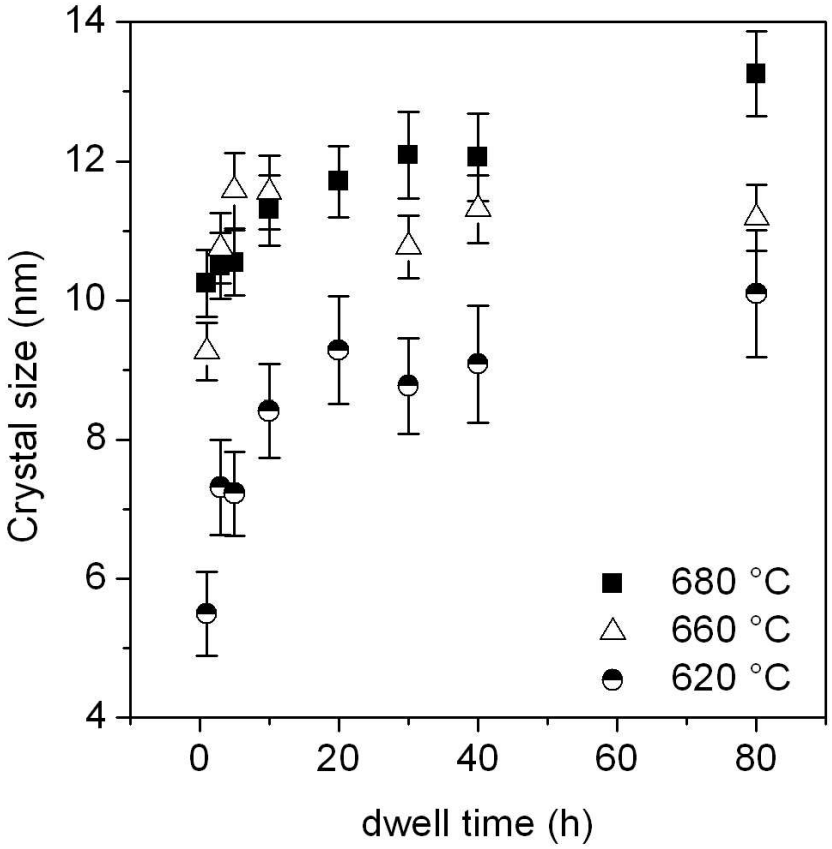

Figure 3: Variation of the crystal size of the glass-ceramics as a function of the time of heat treatment at 620, 660 and 680 °C as calculated on the basis of the (1 1 1) diffraction peak at 27.5° (2θ).
197x203mm (150 x 150 DPI)

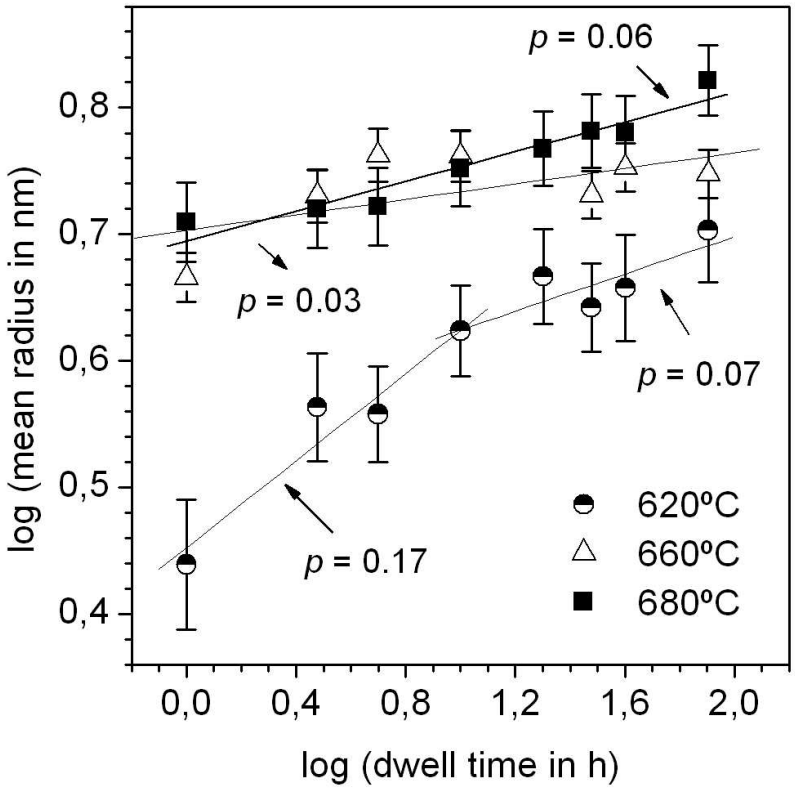

Figure 4: Time-dependent progress of the average crystal radius in double logarithmic scales. The lines provide best fits (Eq. 3) to the data. Numbers indicate growth index p.
206x183mm (150 x 150 DPI)

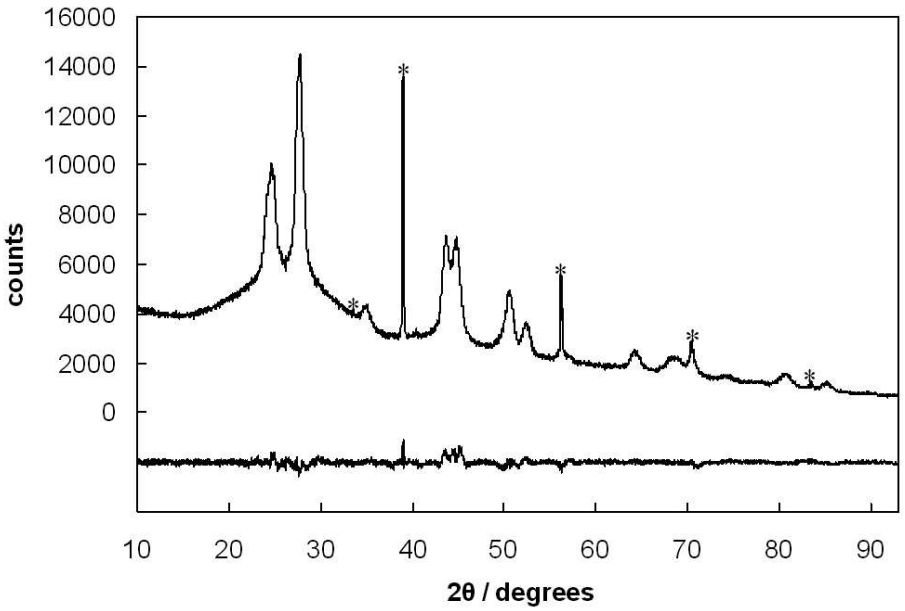

Figure 5: Observed and difference X-ray powder diffraction profiles of glass-ceramic treated at 620 ºC for 40 h with 3 wt.% NaF as internal standard (reflections marked with asterisks).
380x246mm (72 x 72 DPI)

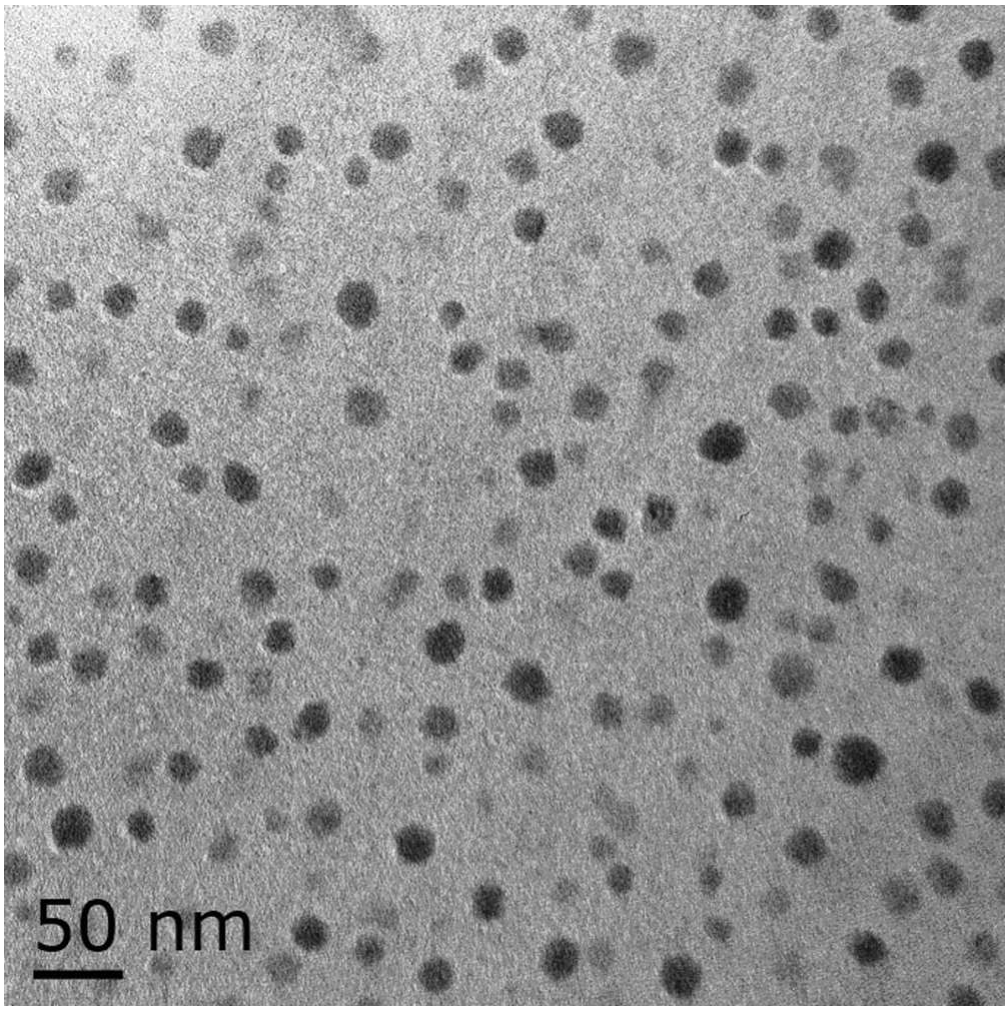

Figure 6a
Figure 6 : Zero-loss filtered bright-field TEM image of (a) the glass sample ,(b) the glass-ceramic obtained at 620 ºC for 40 h and (c) the corresponding La-N4,5 /(Si-L2,3) map.
264x264mm (96 x 96 DPI)

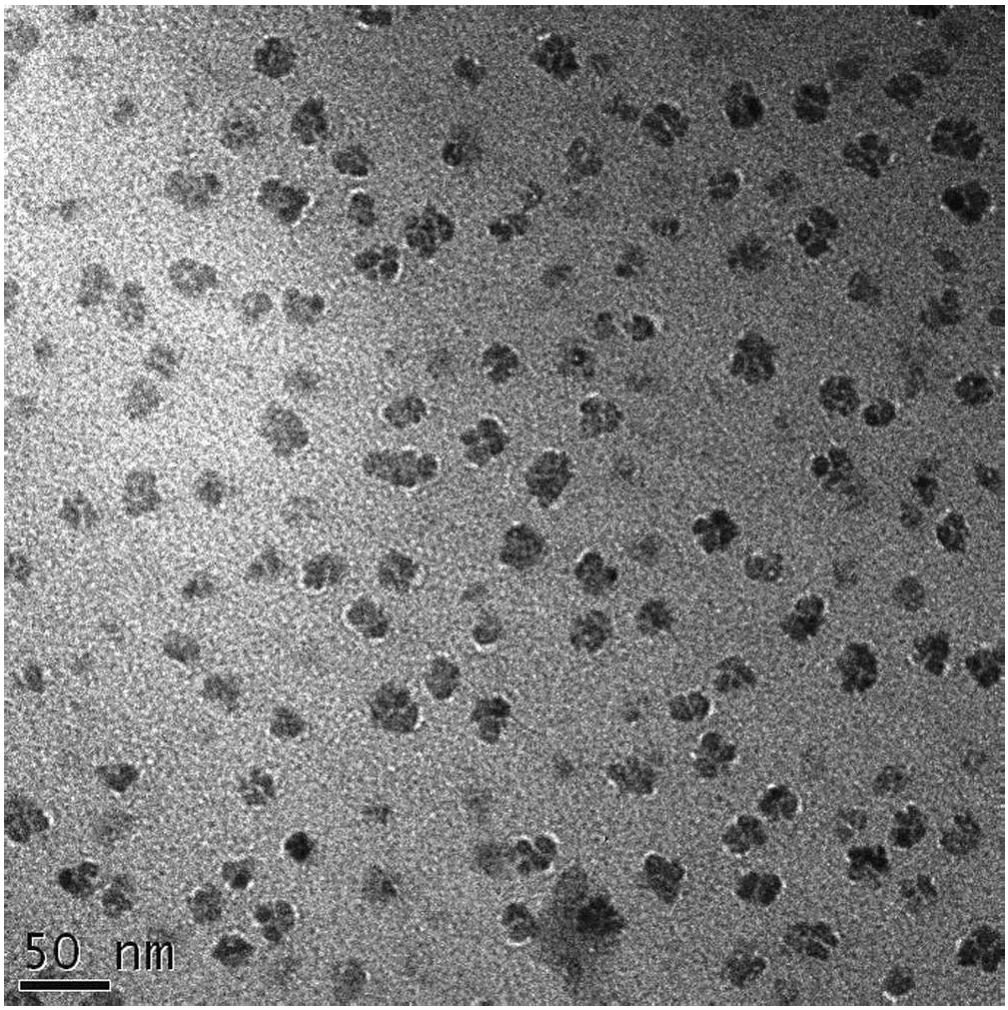

Figure 6b
Figure 6 : Zero-loss filtered bright-field TEM image of (a) the glass sample ,(b) the glass-ceramic obtained at 620 ºC for 40 h and (c) the corresponding La-N4,5 /(Si-L2,3) map.
264x264mm (96 x 96 DPI)

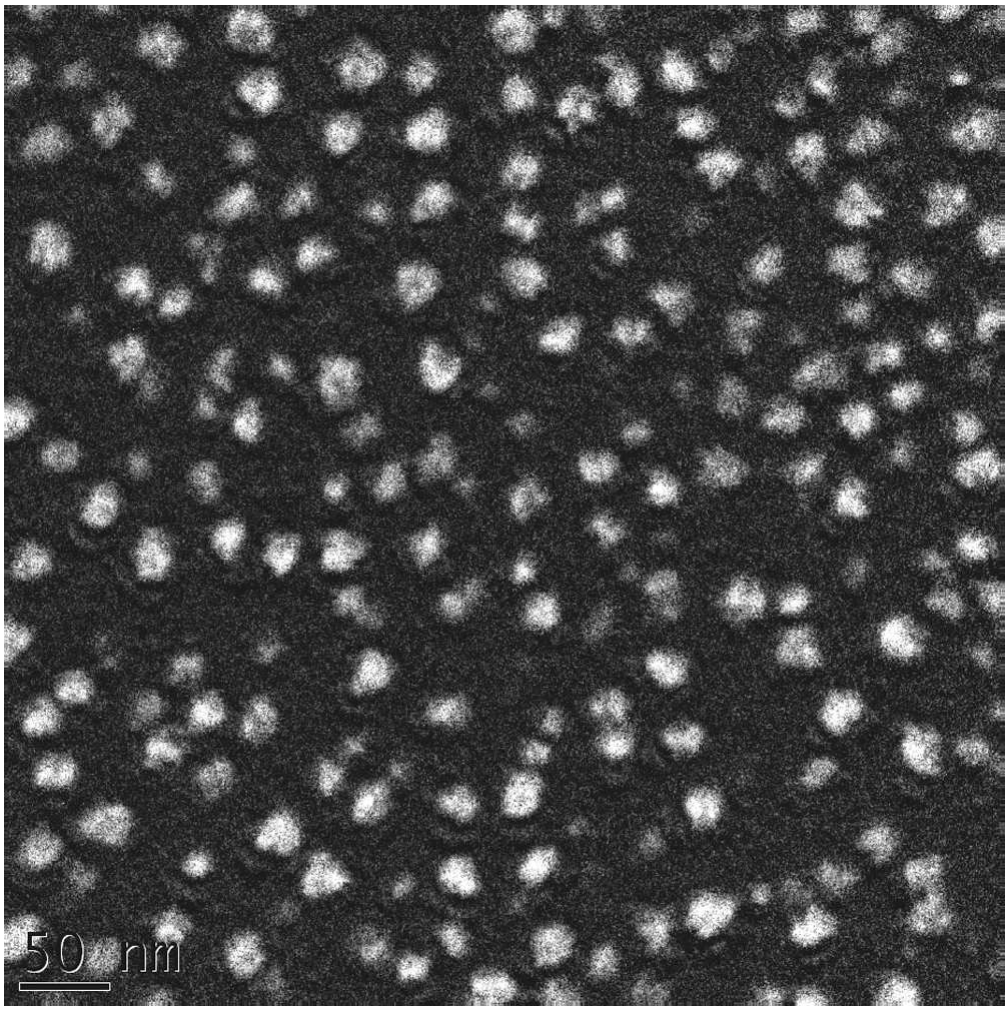

Figure 6c
Figure 6 : Zero-loss filtered bright-field TEM image of (a) the glass sample ,(b) the glass-ceramic obtained at 620 ºC for 40 h and (c) the corresponding La-N4,5 /(Si-L2,3) map.
264x264mm (96 x 96 DPI)

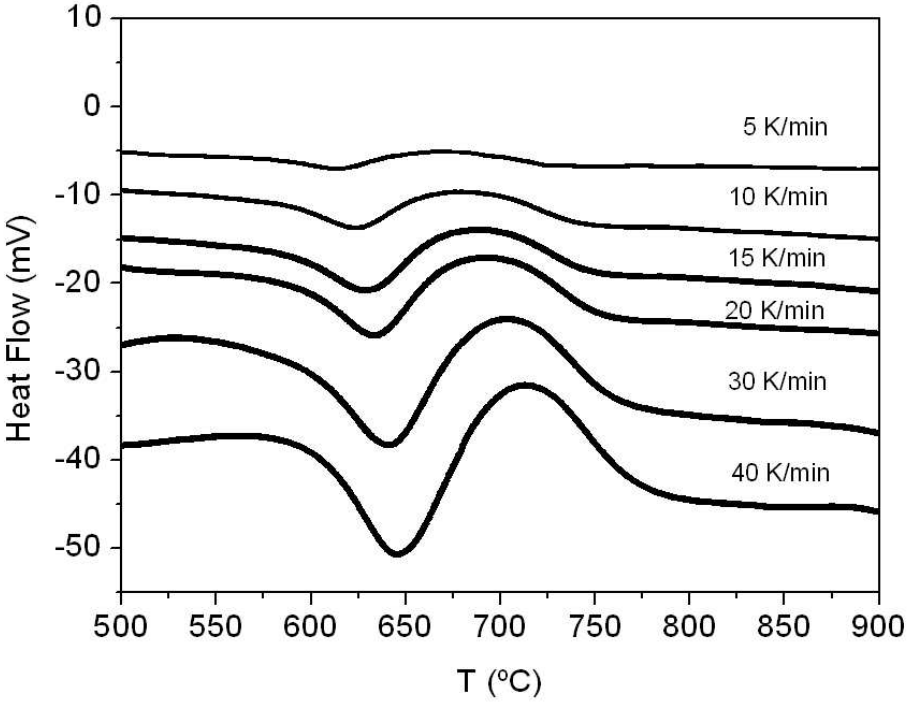

Figure 7: DSC curves of the glass recorded from 5 to 40 K/min.
329x246mm (72 x 72 DPI)

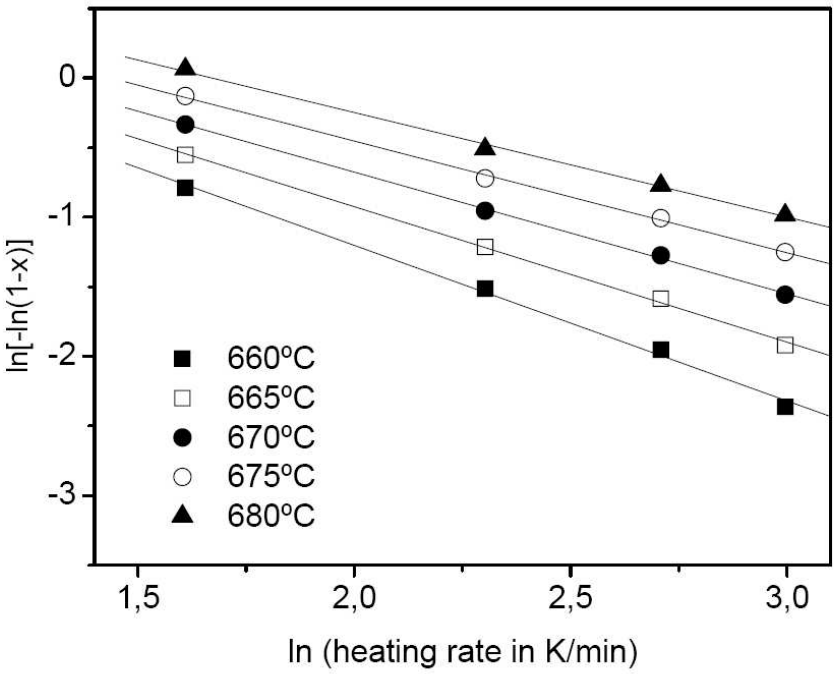

Figure 8: Ozawa plot constructed from DSC data from 660 to 680 ºC for the determination of the Avrami exponent n.
346x252mm (72 x 72 DPI)

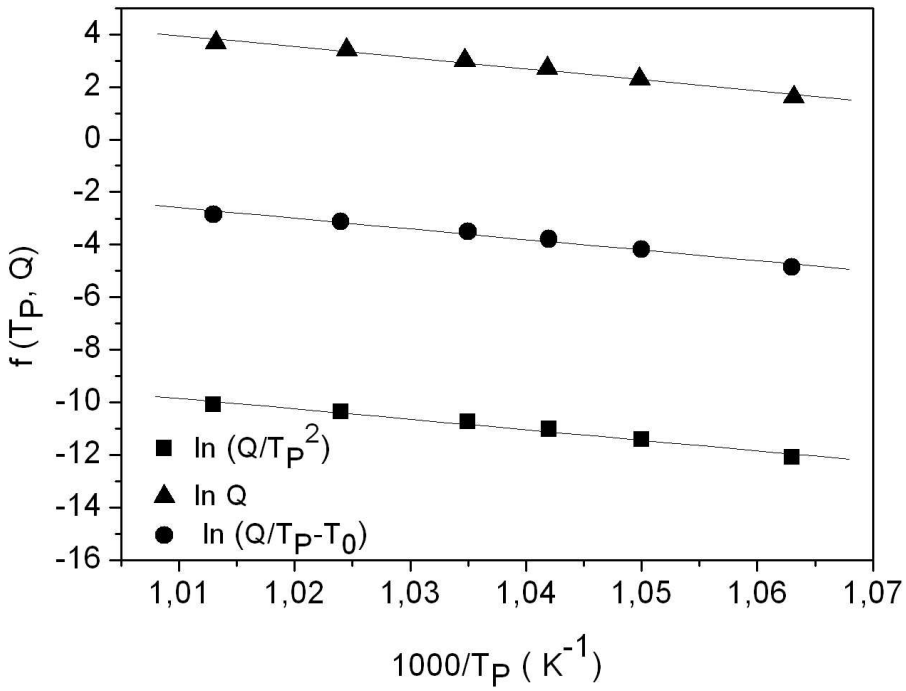

Figure 9a

Figure 9: (a) ■ Kissinger, □ Takhor and ● Augis-Bennett plots constructed from the DSC data; (b) Marseglia and Matusita plots. Q is the heating rate and TP is the DSC crystallisation peak.
238x194mm (150 x 150 DPI)

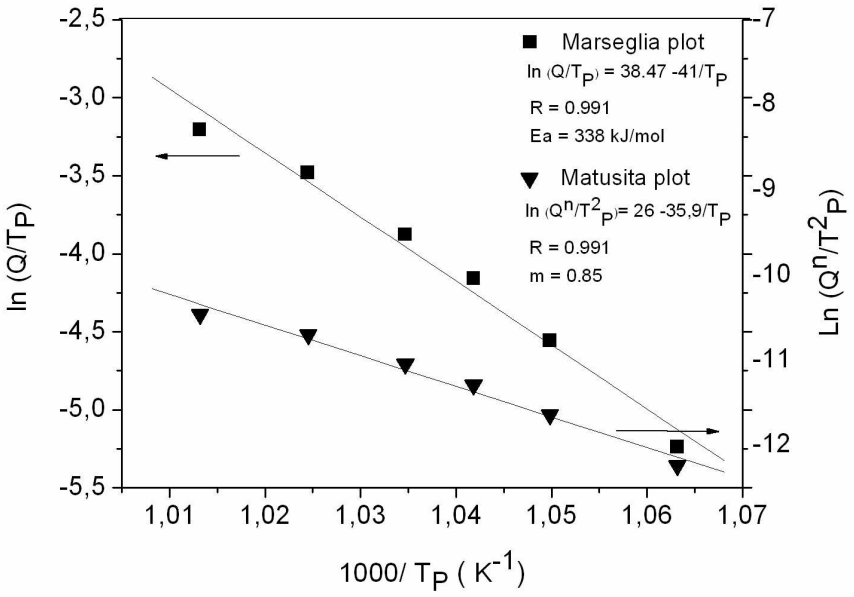

Figure 9b
Figure 9: (a) ■ Kissinger, □ Takhor and ● Augis-Bennett plots constructed from the DSC data; (b) Marseglia and Matusita plots. Q is the heating rate and TP is the DSC crystallisation peak.
283x203mm (150 x 150 DPI)

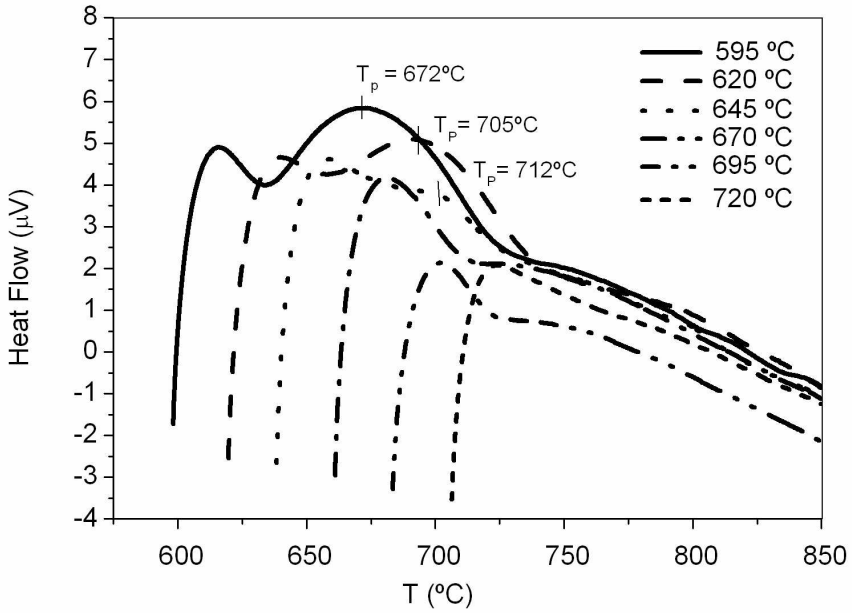

Figure 10: DSC curves of the glass with nucleation temperatures from 595 to 720ºC recorded at a rate of 10 K/min.
296x209mm (150 x 150 DPI)

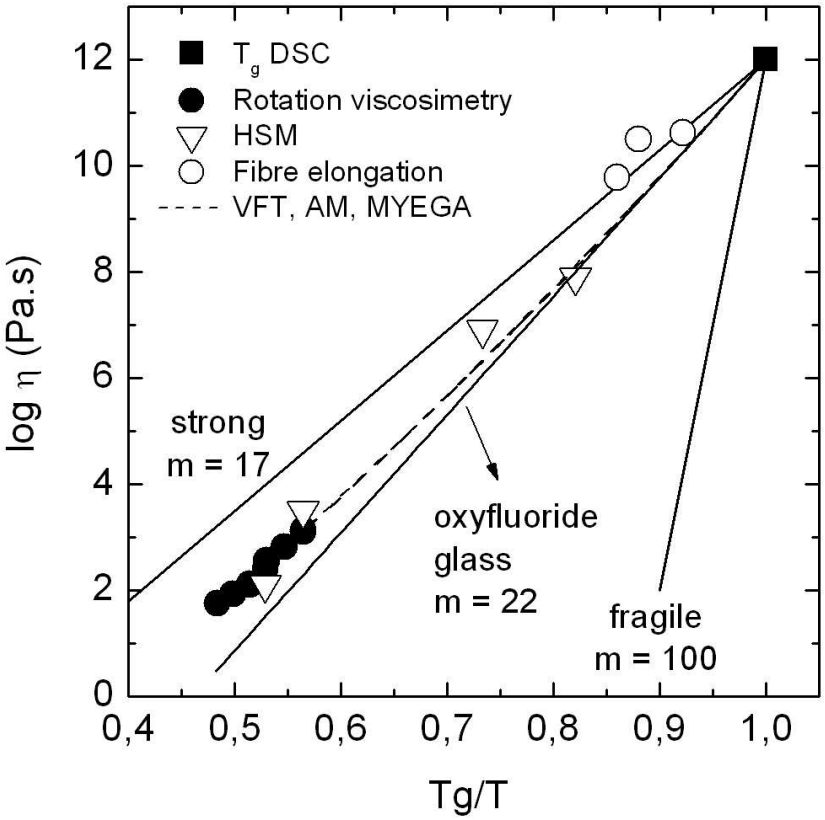

Figure 11: Viscosity-temperature curve of the glass obtained from Tg point, hot-stage microscopy (HSM), fibre elongation and rotation methods. Curves were fitted according to the Vogel-Fulcher-Tamman (VFT), Avramov-Milchev (AM) and Mauro-Yue-Ellison-Gupta-Allen (MYEGA) equations.
201x199mm (150 x 150 DPI)

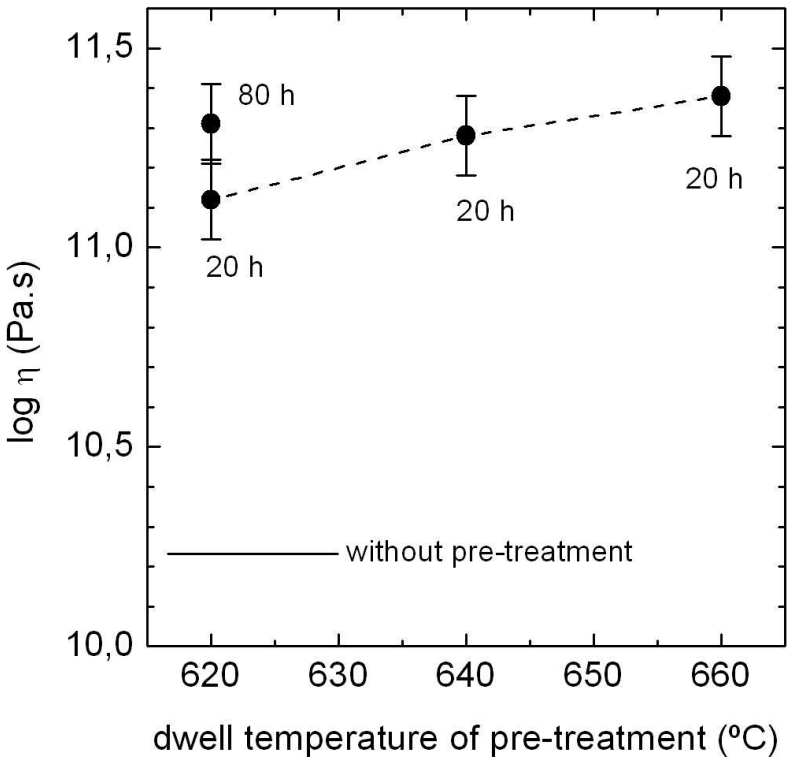

Figure 12. Viscosity of the treated fibres as a function of temperature and time of treatment, measured at 660 ºC.
215x203mm (150 x 150 DPI)

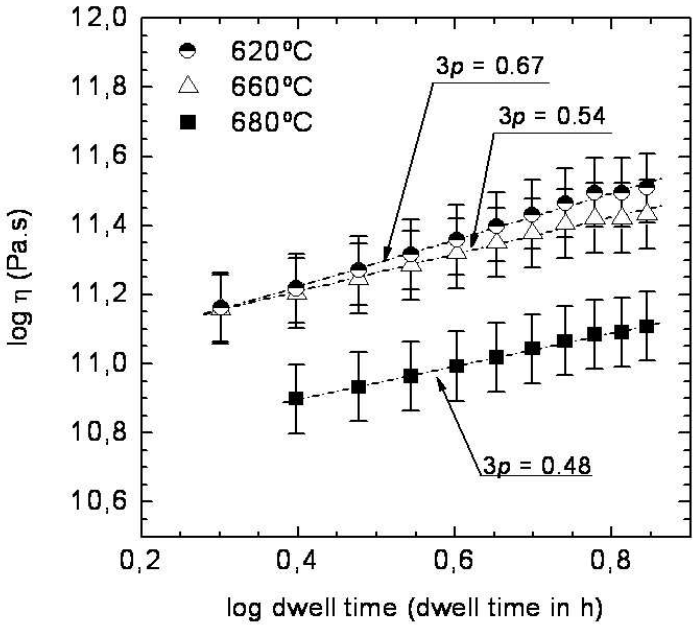

Figure 13: Viscosity as a function of isothermal dwelling at 620, 660 and 680 ºC measured by micro-indentation. Straight lines of slope 3p give the best linear fit to the data.
254x190mm (96 x 96 DPI)